Two-neutrino double-β decay measurement of ^{100}Mo

D. Dassié, R. Eschbach, F. Hubert, Ph. Hubert, M.C. Isaac, C. Izac, F. Leccia, P. Mennrath, and A. Vareille
Centre d'Études Nucléaires, IN2P3-CNRS et Université de Bordeaux, 33170 Gradignan, France

C. Longuemare and F. Mauger
Laboratoire de Physique Corpusculaire, IN2P3-CNRS et Université de Caen, 14032 Caen, France

F. Danevich, V. Kouts, V.I. Tretyak, Yu. Vassilyev, and Yu. Zdesenko
Institute for Nuclear Research of the Ukrainian Academy of Sciences, Kiev, Ukraine

A.S. Barabash, V.N. Kornoukov, Yu.B. Lepikhin, V.I. Umatov, and I.A. Vanushin
Institute for Theoretical and Experimental Physics, Moscow, Russia

C. Augier, D. Blum, J.E. Campagne, S. Jullian, D. Lalanne, F. Laplanche, F. Natchez, G. Pichenot, and G. Szklarz
Laboratoire de l'Accélérateur Linéaire, IN2P3-CNRS et Université de Paris-Sud, 91405 Orsay, France

R. Arnold, J.L. Guyonnet, T. Lamhamdi, I. Linck, F. Piquemal, and F. Scheibling
Centre de Recherches Nucléaires, IN2P3-CNRS et Université Louis Pasteur, 67037 Strasbourg, France

V. Brudanin, V. Egorov, O. Kochetov, A. Nozdrin, Ts. Vylov, and Sh. Zaparov
Joint Institute for Nuclear Research, Dubna, Russia

H.W. Nicholson and C.S. Sutton
Mount Holyoke College, South Hadley, Massachusetts 01075

(NEMO Collaboration)
(Received 29 June 1994)

From data accumulated over 6140 h with 172 g of enriched molybdenum (1.18 mol yr of ^{100}Mo) with the NEMO 2 detector in the Fréjus Underground Laboratory, a clear $\beta\beta2\nu$ signal (1433 events) is observed, leading to a half-life, $T_{1/2} = 0.95 \pm 0.04(\text{stat}) \pm 0.09(\text{syst})\ 10^{19}$ yr. The experimental two-electron energy spectrum and the two-electron angular distribution are in agreement with the expected ones. Limits for $\beta\beta0\nu$ decays to the ground state, excited states (2_1^+ and 0_1^+), and also with Majoron emission are given.

PACS number(s): 23.40.Bw, 14.60.Pq

I. INTRODUCTION

$\beta\beta0\nu$ decay can occur if the neutrino is a massive Majorana particle, i.e., if it is its own antiparticle so that lepton number conservation is violated and neutrino exchange between two nucleons can take place with the emission of only two electrons. If only left-handed currents are present, the transition is possible because the Majorana mass term can flip the chirality of the emitted left-handed neutrino to a right-handed neutrino which is absorbed. Therefore, the observation of a $\beta\beta0\nu$ transition would prove the Majorana nature of the neutrino.

In the study of double-β decay processes nuclear physics is important because one cannot have predictions for the fundamental parameters such as the neutrino mass or the coupling to possible right-handed currents in the weak interaction if there are no reliable calculations of the nuclear matrix elements. Many efforts have been devoted to clarify the mechanism by which these processes occur and to perform calculations of the nuclear structure which enters the half-life formulas. As far as the $\beta\beta2\nu$-allowed process is concerned, a half-life can be measured and nuclear matrix element calculations can be tested. Although there are no clear relations between the matrix elements of the two processes ($\beta\beta2\nu$ and $\beta\beta0\nu$), comparisons with experiments in the case of the allowed process may give some confidence in the computations.

During the past four years the NEMO Collaboration has built two detectors NEMO 1 [1] and NEMO 2 [2,3] in a research and development effort devoted to the measurement of the two-electron background in the 3 MeV region ($Q = 3.03$ MeV for the ^{100}Mo $\beta\beta0\nu$ decay). Toward this end, the NEMO 2 detector was installed in the Fréjus Underground Laboratory [4800 meters of water equivalent (m.w.e.) depth] in August of 1991. The $\beta\beta2\nu$ signal reported here is a by-product of this research and preliminary results [4] have already been presented with a fraction of the current data sample. The collaboration is now building a new detector called NEMO 3 [5] which will be able to accommodate up to 10 kg of enriched molybdenum and/or other double-β-decay candidates to

study $\beta\beta0\nu$ decay and to probe the effective Majorana neutrino mass at the level of 0.1 eV in order to improve by an order of magnitude the present limits.

In the following, the NEMO 2 detector and its performances are described. After a discussion of background studies, the method for extracting the $\beta\beta2\nu$ signal is explained and half-life limits for 0ν modes are presented. In the conclusion, the results are compared to recent published values and to theoretical predictions. Limits on the effective neutrino mass and Majoron coupling are derived with recent calculations of matrix elements.

II. NEMO 2 DETECTOR

A. Experimental setup

The active detector [2,3] (Fig. 1) consists of two parts. The first one is the tracking volume of 1 m^3 filled with helium gas. The second one is a calorimeter made of scintillators covering two sides of the cube. In the detector the track topology, the energy, and the timing of charged particles are recorded while photons are also detected. For the materials used in the construction of the detector samples were measured using low background Ge detectors [6] in order to select materials with activities less than 10 mBq/kg. The photomultiplier tubes (PMTs) were not of low activity and generated most of the external photon flux. The tracking and calorimeter parts of the detector are shielded by iron (20 cm) and lead (5 cm).

1. Tracking device

The tracking volume of the detector consists of octagonal cells identical to those of the previous detector NEMO 1. Each cell has one central wire surrounded by eight ground wires which are 100 μm diameter nickel wires. The cells are 32 mm in diameter and 1 m in length. On both ends there is a copper ring used as a pickup electrode for the cathode. Helium gas, with 4% ethyl alcohol, fills the detector at atmospheric pressure. The average density of gas in the sensitive volume is 0.2 mg/cm^3 which yields an energy loss of 16 keV for a 500 keV electron traveling through 50 cm of the detector. This provides the tracking of electrons with energies as low as 100 keV with an efficiency in each cell greater than 99%. The wire cells work in the Geiger mode, the electrons drift toward the central wire at a speed of 1 cm/μs, and the avalanche near the wire develops into a plasma which propagates along the wire at a speed of 6 cm/μs. Pickup electrodes near the ends of the anode wire detect the propagating plasma.

In the NEMO 2 detector the source plane (1 m$\times$1 m) splits the 1 m^3 tracking volume into two equal parts. Each part is formed by five frames of 2×32 Geiger cells. A frame is made of two crossed planes of cells orientated vertically and horizontally. The tracking volume is closed by two sheets of aluminized mylar (36 μm) in front of the calorimeter. In addition to recording the $\beta\beta$ decay

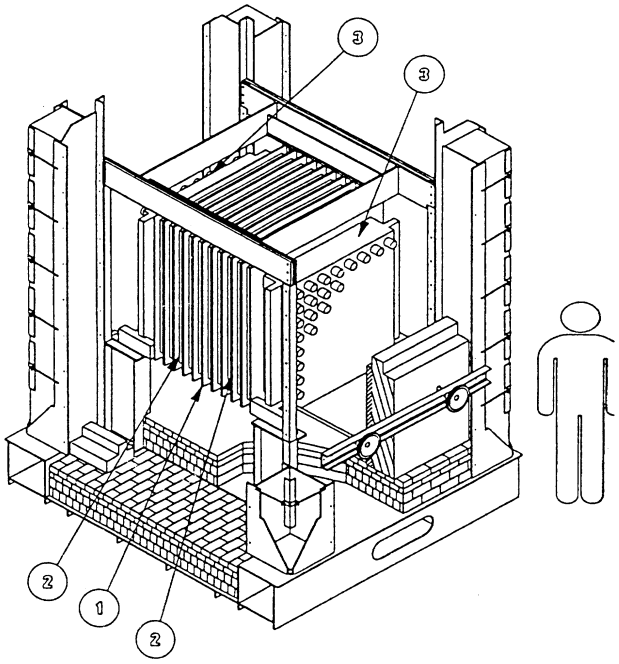

FIG. 1. The NEMO 2 detector. (1) Central frame with the metallic foil. (2) Tracking device of 10 frames with 2×32 Geiger cells each. (3) Scintillator array of 8×8 counters. (The shielding is not shown.)

prompt signals, a measurement of delayed Geiger cell signals (up to 1 ms after a trigger) allows one to quantitatively identify the presence of ^{214}Bi decaying into ^{214}Po which emits an α particle with a half-life of 164 μs.

2. Calorimeter

On each side of the tracking volume is an array of 64 scintillation counters. Each one (12 cm $\times$ 12 cm $\times$ 2.25 cm) is made of 2 cm of plastic scintillator and a 2.5 mm layer of CsI(Na). The CsI(Na) signal has a 400 ns decay constant and is readily isolated from the scintillator signal. The photon detection efficiency is 15% at 500 keV and electrons with kinetic energies up to 4 MeV are stopped in the scintillator. The front face of the scintillators is covered with polycarbonate and Teflon to protect them from ambient light and to optimize light collection. The thickness of these materials corresponds to 4.6 mg/cm^2 of Mylar. A 500 keV electron loses 45 keV when leaving the tracking volume and entering the scintillator.

The two scintillator arrays are devoted to energy and time-of-flight measurements. The measurement of the performances of the scintillation counters is crucial for event selection and background rejection. The scintillation counters have a detection threshold set at 50 keV.

3. Molybdenum sources

The source foil studied since January 1993 is divided in two parts. The first part consists of enriched molyb-

denum (98.4% in ^{100}Mo) with a fiducial mass of 172 g and the other is natural molybdenum (163 g) which has a ^{100}Mo isotopic abundance of 9.6%.

The molybdenum sources were produced by ITEP (Moscow). The natural molybdenum was manufactured from monocrystals that were grown via a vacuum zone smelting technique to ensure very high purity material. Enriched molybdenum powder was smelted by an electron beam to provide the material for the enriched foil. In the final stage both the natural and enriched metallic foils were formed on the same equipment using a standard rolling technology. The enriched molybdenum foil was made from 12 strips placed side by side with an average thickness of 40 μm and a measured dispersion ≤ 4 μm. The natural molybdenum foil was five strips 44 μm thick with a measured dispersion ≤ 2 μm.

The experiment in two previous phases [7,3] used a high purity copper foil and commercial natural molybdenum foils in order to study the background due to the external photon flux and the detector's response to contamination in the source foil.

B. Detector performances

1. Charged particle tracking

Each cell provides three-dimensional measurements of charged particle tracks by recording the drift time and two plasma propagating times. The drift time is used to measure the transverse position and the plasma propagation times are used to measure the longitudinal position. Using cosmic rays, a relationship was established between the drift time and the distance of the trajectory from the central wire. The longitudinal position is deduced from the difference in the timing signals received at both ends of the cathode wires. The average transverse resolution is 500 μm and the longitudinal resolution is 4.7 mm.

As low energy electrons are involved, multiple scattering effects in the helium gas as well as interactions with the wires have to be taken into account, and so a pattern recognition code has been developed using a method based on the Kalman filter [8]. This program provides the parameters of the tracks.

2. Energy and time calibrations

Absolute energy calibrations are performed using radioactive sources (^{207}Bi, ^{137}Cs, and ^{88}Y) placed in front of each of the 128 scintillators. The deduced energy resolution full width at half maximum (FWHM) (keV)$=\sqrt{28E(\text{keV})+2300}$ yields a value of 17.4% at 1 MeV. To check the stability of the scintillation detectors, a laser and fiber optics device was used. In this device laser light is sent via plastic optical fibers to each detector and to reference counters. The intensity is varied by introducing neutral density filters of different known transmissions to simulate the full range of energy deposited in the scintillators. This method provides a daily check on the linearity of the detector response. Laser stability is checked by a photodiode reference counter. The photodiode simultaneously records the signal from a few fibers and from an ^{241}Am source of α particles for self-calibration. The long term precision of this calibration procedure is estimated at 4% (systematics included).

In the laser calibration process the light intensity is varied and a measure of time versus energy is acquired. The corresponding time-versus-charge instrumentation dependence is due to the use of leading edge discriminators and has been parametrized with four parameters for each counter, taking into account the pulse shape, $T(qdc) = p1 - (p2/qdc) - (p3/qdc)\exp(-p4/qdc)$. Here qdc is the measured charge of the signal. The relative timing offsets for each channel were determined with a ^{60}Co source placed in the center of the detector. The time resolution (rms) of each counter is approximately 250 ps at energies greater than 1 MeV but reaches 450 ps at 200 keV, with the long term stability limited to 200 ps drifts after software corrections.

3. Data acquisition

The trigger for data collection requires that at least two scintillation counters generate signals within 50 ns followed by four Geiger frames fired within 2.5 μs. The typical trigger rate is 0.25 Hz. Several other trigger configurations are available for data collection, electronics tests, and calibration procedures. A microprocessor connected to a micro-VAX is used for acquisition, formatting, calibrating, and filtering the data. The filtering reduces the data by a factor of 30 and is based on timing criteria and event reconstruction. To check the filtering procedure unfiltered data are recorded for analysis on a regular schedule.

4. Definition of events and cuts

An electron is defined by a track linking the source foil and one scintillator; the maximum scattering angle along the track has to be less than 20°. The interaction of a photon is recognized as one or two adjacent scintillators which fire without an associated particle track, while an associated CsI is acceptable. The CsI signal is mainly used as a veto. A deposited energy greater than 200 keV is required in at least one plastic scintillator, for photons and electrons, in order to obtain a time resolution better than 500 ps.

In the coordinate system of NEMO 2 the origin of the axes is located at the center of the detector, the z axis being perpendicular to the foils, the x axis horizontal and the y axis vertical. The enriched molybdenum area is defined by an x-vertex position inside the range -47.5–2.5 cm and the natural molybdenum by an x vertex inside the range 4.5–47.5 cm. In both cases the y-vertex position is within the limits -46.0–46.0 cm (Fig. 3). In the analysis, the electron-electron ($2e$) and electron-photon ($e\gamma$) events were intensively studied; see Fig. 2. In the case of $2e$ events, the difference between the vertex posi-

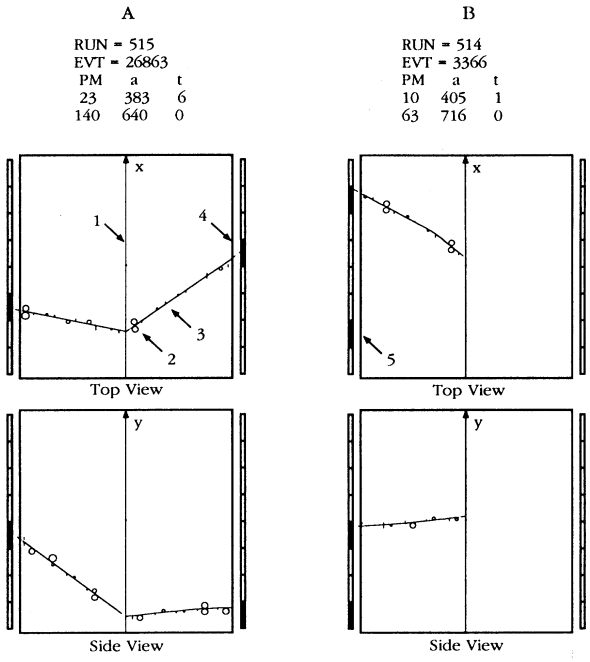

FIG. 2. Typical events in NEMO 2. (A) $2e$ event. (B) $e\gamma$ event. (1) Source plane. (2) For the Geiger cells perpendicular to the figure plane, the drift distance is given by the diameter of a circle, and the electron trajectory is tangent to the circles. (3) For the Geiger cells parallel to the figure plane, the small segments indicate the trajectory position along the wires. (4) Fired counters associated with the track. PMT information (a) deposited energy in keV and (t) time in tenths of ns with respect to the first fired counter. (5) Fired counter due to a photon.

tion of each track was required to be less than 5 cm; this condition was imposed due to multiple scattering which leads to a rms of 1 cm for a 200 keV electron. Interestingly enough no $2e$ events are rejected with this cut and a much looser cut would not introduce background events.

III. SIMULATIONS

Monte Carlo simulations have been carried out using GEANT (version 3.15) [9]. The $\beta\beta2\nu, \beta\beta0\nu$ decays to the ground and excited states and $\beta\beta$ decay with Majoron emission have been simulated. Theoretical formulas [10] were used with the appropriate Primakoff-Rosen approximation for molybdenum. An efficiency for the $\beta\beta2\nu$ mode of 2.8% was found after applying the previously defined cuts. The low efficiency is mainly due to the detector geometry and to the electron energy cut at 200 keV.

Decays of radioactive nuclei which can be sources of background in double-β-decay were also studied. The decays studied accurately represent nuclear schemes [11], and internal conversion coefficients were calculated when experimental values were unknown. ^{234m}Pa (Q = 2.2 MeV), ^{214}Bi (Q = 3.3 MeV), and ^{208}Tl (Q = 5.0 MeV) were found to be the main contaminants and the last two are also sources of background in the 3 MeV region for $\beta\beta0\nu$.

In the first phase of the experiment, the foil had contamination levels measured by germanium spectroscopy to be 1.5 Bq/kg of ^{214}Bi and 0.1 Bq/kg of ^{208}Tl. These known levels provided an excellent check on the consistency of the code with the observed behavior of the detector [3].

IV. TWO-ELECTRON BACKGROUND SOURCES

There are two possible origins of $2e$ background events which are emitted from the source foil. The first category called "external" background, is caused by electrons or photons generated outside of the source foil and interacting with the detector. Most of the photons produce, via the Compton effect, electrons which may escape the scintillators and cross the tracking device. Such events are rejected by time-of-flight analysis.

Depending on their energy, photons interacting with the source foil produce Compton electrons or e^+e^- pairs. A Compton electron can be associated with a secondary electron by Møller scattering or by a second Compton effect. This background cannot be rejected by time-of-flight criteria.

The second category of background is the "internal" one and is due to the presence of radioactive nuclei inside the source foil; most of these nuclei are β emitters. A secondary electron can occur by internal conversion; it can also be created by the Compton effect from photons of the cascades or from the Møller effect.

A. External background

The external photon flux is mainly due to the radioactivity in the PMT's glass (1800 Bq/kg of ^{40}K and 25 Bq/kg of ^{214}Bi). Most of the $e\gamma$ events are produced by the Compton effect in the foils, giving rise to the detection of one electron and one photon. When the incoming photon interacts in the scintillators it can generate also $e\gamma$ events if the electron escapes from the scintillator and stops in the foil. Internal and external timing hypotheses are compared and the one corresponding to the most probable topology is selected. The vertex distributions for the $e\gamma$ events are shown in Fig. 3. The decreasing population toward the edges of the source foil is due to the geometrical acceptance.

The distributions of the angle between the photon and the electron have the same behavior in both foils (Fig. 4) and show the dominance of the Compton effect giving rise to an asymmetry. The $E_e + E_\gamma$ energy distributions (Fig. 5) in both foils have also very similar shapes, showing the large contribution of ^{40}K (E_γ=1.46 MeV) in the photon flux. A small number of events with higher energies is most likely from ^{208}Tl and ^{214}Bi in the PMT's glass and from residual radon around the tracking device. The Monte Carlo simulation of these photons reproduces rather well the observed $e\gamma$ angular distribution and the $e\gamma$ energy spectrum but not in its high energy tail. The

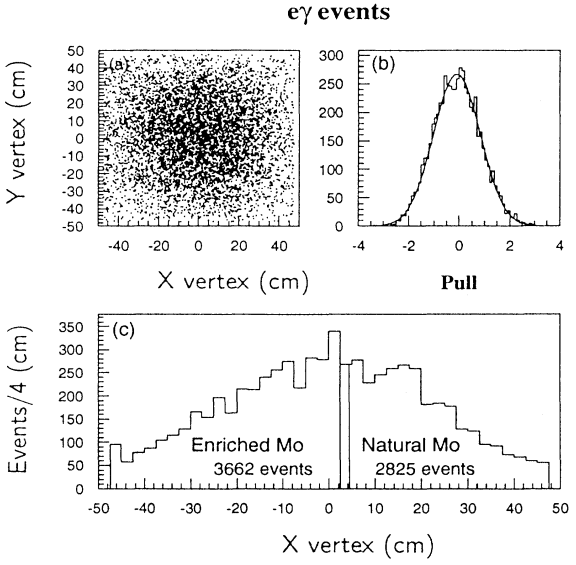

FIG. 3. Vertex and pull distributions. The vertex distribution (a) does not exhibit different behaviors in enriched and natural molybdenum. In the X-vertex distribution (c) the two fiducial zones are indicated. The decrease of the efficiency with the increasing distance from the center is due to the geometrical acceptance. The pull (b) defined by $(dt_{\text{expt}} - dt_{\text{int}})/\sqrt{\sigma^2_{\text{expt}} + \sigma^2_{\text{int}}}$ where dt is the time difference between the detected electrons, has the expected distribution, expt and int refer, respectively, to experimental data and to calculation in the internal hypothesis.

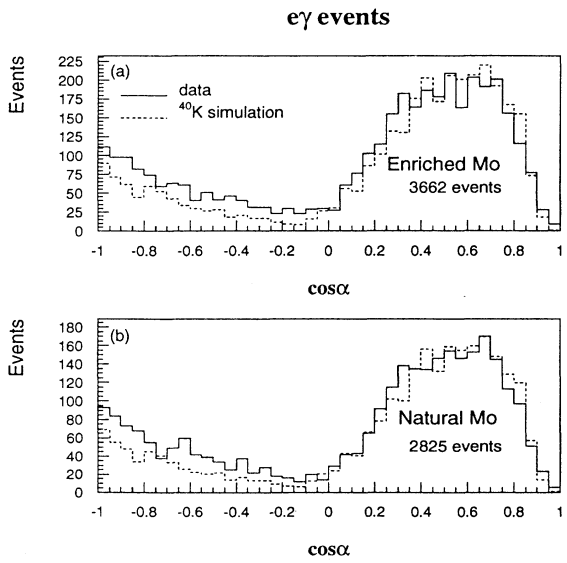

FIG. 4. Angular distributions. α is the angle between the electron and photon directions. The angular distributions strongly favor the forward direction, indicating the dominance of the external photon flux. The simulation of $e\gamma$ events induced by ^{40}K in the PMT's glass superimposed on the enriched molybdenum spectrum (a) and on the natural molybdenum spectrum (b) accounts for the shapes of the spectra.

detailed model of the external photon flux crossing the foils cannot be estimated with sufficient accuracy to reproduce the high energy $e\gamma$ events and accordingly the $2e$-induced events in both foils. So the experimental $2e$ data in natural molybdenum were used to estimate the external $2e$ background in the enriched molybdenum.

B. Internal background

The internal background contribution of $e\gamma$ events in the foil can be deconvolved from the external photon flux through considerations of back-to-back events where an electron is detected on one side of the source and a photon on the other side ($\cos\alpha < 0$) (Fig. 4). The most energetic part of the γ energy spectra, which is not well populated with the external photon flux events, is well suited for ^{208}Tl and ^{214}Bi activity measurements. Upper limits for ^{208}Tl and ^{214}Bi contamination were computed, at the 90% confidence level using Poisson statistics.

In the following the detection efficiencies (ϵ) of various channels are given for the enriched molybdenum foil. In the case of ^{208}Tl, a simple cut suggested by simulations, $E_e + E_\gamma > 2.5$ MeV ($\epsilon = 3.1 \times 10^{-4}$), gives two

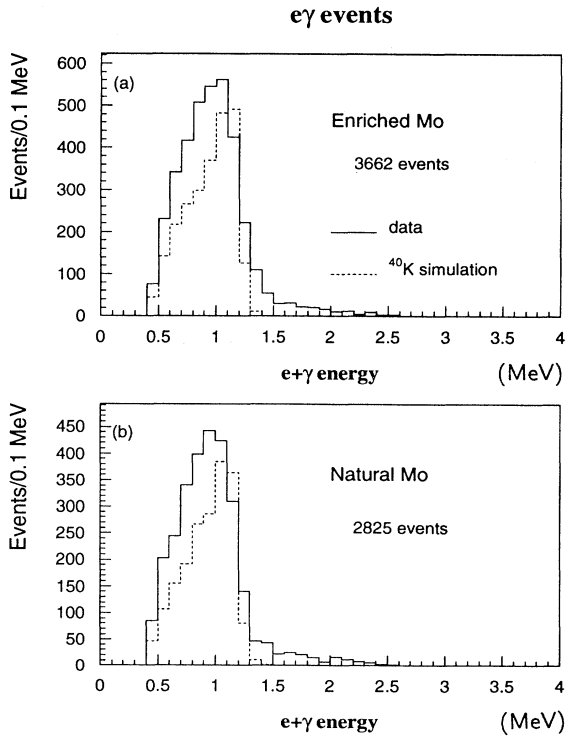

FIG. 5. $E_e + E_\gamma$ energy distributions. In the $E_e + E_\gamma$ energy distributions the peak is due to two effects: the strong contribution of ^{40}K to the external photon flux and the energy cuts. There is also a contribution of higher energy photons. The distributions in enriched (a) and natural (b) molybdenum have very similar shapes reflecting similar photon fluxes. The simulation of $e\gamma$ events induced by ^{40}K in the PMT's glass accounts for the Compton edge of the experimental spectra.

and one experimental events detected in the enriched and natural molybdenum foils, respectively. Upper limits of 4.4 mBq/kg and 4.0 mBq/kg are thus deduced. This level of contamination would produce 17 and 15 $2e$ events, respectively ($\epsilon = 1.1 \times 10^{-3}$), for the duration of the experimental exposure.

In studies of the ^{214}Bi contamination, the entire range of the photon spectrum is populated by events coming from the external photon flux. However, using two cuts $1.1 < E_\gamma < 1.9$ MeV and $1.6 < E_e + E_\gamma < 2.4$ MeV, the calculated limit is optimized. Within these cuts ($\epsilon = 2.3 \times 10^{-4}$), 22 events remain in the enriched molybdenum and 13 events in natural molybdenum, leading to upper limits of 33 and 23 mBq/kg. Such contaminations levels would produce 90 and 59 $2e$ events, respectively ($\epsilon = 0.7 \times 10^{-3}$). A 400 h measurement, with a germanium detector, of 270 g of the same sample of enriched molybdenum has given upper limits of 5 mBq/kg (^{208}Tl) and 50 mBq/kg (^{214}Bi). The 450 h measurement of a 170 g sample of natural molybdenum has given similar limits.

Another source of background is pure β emitters producing $2e$ events by the Møller effect. A special "one-counter-only" trigger was invoked for a short run time of 64 h in order to search for emitters such as ^{234m}Pa and ^{90}Y ($Q \sim 2.3$ MeV) from ^{90}Sr. The X-vertex distribution of these events (Fig. 6) does not show a noticeable difference between the molybdenum foils. Analyzing the electron spectra in enriched and natural molybdenum, for $E_e > 1.2$ MeV, and assuming these spectra are dominated by ^{234m}Pa decays ($\epsilon = 0.61 \times 10^{-3}$), one finds contaminations of 66 ± 5 mBq/kg and 86 ± 7 mBq/kg, respectively, by fitting the experimental spectra to a simulated ^{234m}Pa energy spectrum. An upper limit of 41 $2e$ events ($\epsilon = 0.3 \times 10^{-3}$) due to single-$\beta$-emitters in the enriched molybdenum foil was deduced after background subtraction using the natural molybdenum data.

C. Neutron-induced events

Neutron capture in materials surrounding the tracking volume is followed by photon emissions with energies up to 8 MeV. High energy "$2e$ events" are expected by pair production in the 3 MeV region, where the pair production process has a much greater probability than the second order processes Compton plus Møller or double Compton. In order to study the neutron-induced events, an Am-Be neutron source was placed near but outside of the shielding for 3.6 h. To present a nearly uniform neutron flux the source was located in the plane of the molybdenum foils at a distance of 2.5 m. Then assuming the interactions associated with the neutron source produce events similar to those of the residual neutron flux in the laboratory, the analysis of $2e$ and single electrons crossing the foils shows that this short exposure corresponds to a run of 10 yr under the normal data collection mode. The $2e$ event rate due to the residual neutron flux of about 0.2 events/MeV yr is deduced in the 3 MeV region and is negligible for the $\beta\beta 2\nu$ mode.

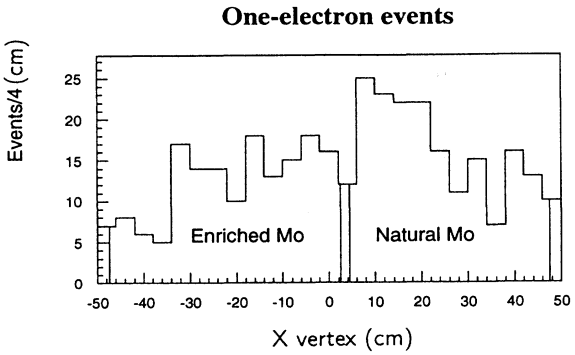

FIG. 6. Electron vertex distribution. The selected electrons in the one-track trigger run (64 h) have an energy greater than 1.2 MeV; this cut allows limits to be put on the different contaminations for single-β-emitters such as ^{234m}Pa and ^{90}Sr/^{90}Y.

D. Events due to radon

Radon is outgassed into the air from the rocks. The contributing daughter to background events is ^{214}Bi. The usual radon measurement in the underground laboratory gives 20 Bq/m^3 but it has reached as high as 100 Bq/m^3 during a period of poor ventilation in the laboratory. Accordingly there was an increase in the trigger rate from 0.23 Hz to 0.31 Hz. This period with fluctuations in the radon rate occurred for less than 10% of the total run time. From the analysis of the data with the high radon level of 100 Bq/m^3 (510 h), the radon contribution to $e\gamma$ and $2e$ counting rates under standard conditions (20 Bq/m^3) is found to be 0.2/h and 0.01/h, respectively, in the two foils.

V. RESULTS

The $2e$ event selection is based on time-of-flight analysis (Fig. 7); for each event a hypothesis is made as to the internal (int) or external (ext) nature of an event. From the calculated χ^2 a probability is deduced for each case, $P_{\rm int}$ and $P_{\rm ext}$. Cuts requiring $P_{\rm int} > 10^{-2}$ and $P_{\rm ext} < 10^{-5}$ have been applied to identify internal events. The pull $[(dt_{\rm expt} - dt_{\rm int})/\sqrt{\sigma^2_{\rm exp} + \sigma^2_{\rm int}}$ where "expt" means experimental and dt refers to the time difference between both electrons] has the distribution of selected events shown in Fig. 8 and exhibits the expected centered and normalized Gaussian behavior. The raw data are presented in Figs. 9(a) and 10(a) for natural and enriched molybdenum. The $2e$ energy spectrum in the natural molybdenum foil contains 642 events. The calculated $\beta\beta 2\nu$ contribution using a consistent half-life limit is shown. The ^{214}Bi contribution using the upper limit of 33 mBq/kg is also indicated here and is shown to be insignificant relative to the external background. By subtracting the $\beta\beta 2\nu$ contribution and letting the ^{214}Bi-dominated internal contribution be addressed in terms of systematic errors, a spectrum for the background events is derived, Fig. 10(a).

The $2e$ energy sum spectrum in the enriched molybdenum foil with 1947 events is shown in Fig. 10. A two-parameter fit of the data is made involving the background spectrum and the simulated $\beta\beta2\nu$ spectrum. The fit indicates that there is an external event background spectrum with 514 events which is derived from the background spectrum in natural molybdenum with a normalization factor of 1.0 ± 0.15. The background was then subtracted bin per bin yielding 1433 events in the $2e$ spectrum.

A. $\beta\beta2\nu$ signal

A χ^2 fit [12] to the ^{100}Mo $2e$ energy spectrum (Fig. 11) using the $\beta\beta2\nu$ simulation spectrum and letting the half-

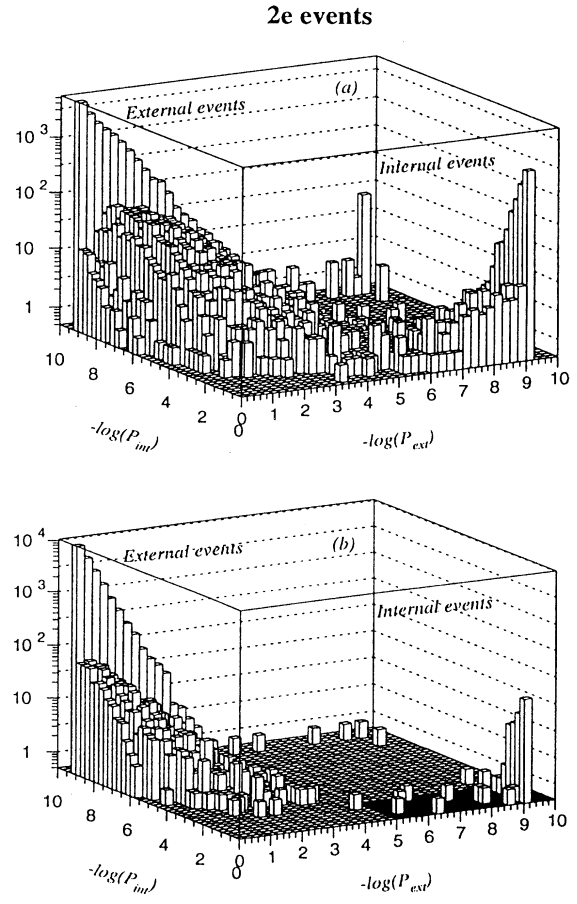

FIG. 7. Probability distribution of $2e$ events. For each event an internal hypothesis and an external hypothesis are made (see Sec. IV) the corresponding χ^2 are calculated, and the decimal logarithm of the deduced probability is plotted. The internal event selection requires $P_{\rm int} > 10^{-2}$ $[-\log_{10}(P_{\rm int}) < 2]$ and $P_{\rm ext} < 10^{-5}$ $[-\log_{10}(P_{\rm ext}) > 5]$; the black area in (b) shows the domain of the selected events. Filtered data (a) and a sample (b) of nonfiltered data (260 h) are presented, a very clear separation between internal and external events is obtained, and less than ten external events are expected in the selected internal $2e$ events.

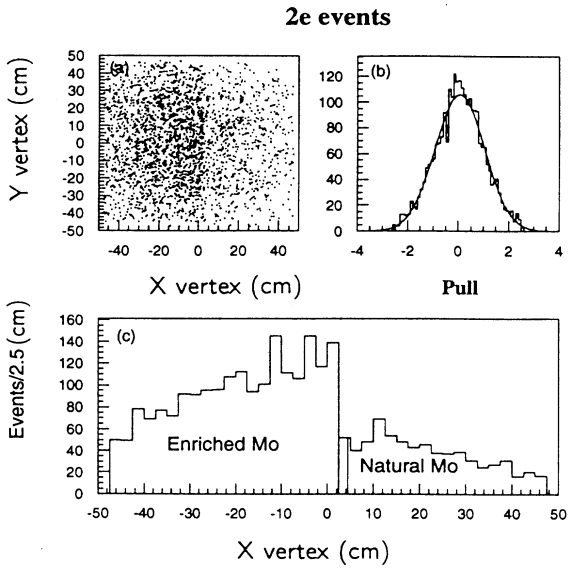

FIG. 8. Vertex and pull distributions. The vertex distributions (a) and (c) show clearly a large difference between enriched and natural molybdenum. The pull distribution (b) $(dt_{\rm exp} - dt_{\rm int})/\sqrt{\sigma^2_{\rm expt} + \sigma^2_{\rm int}}$ of the selected events has the expected behavior, a centered and normalized Gaussian.

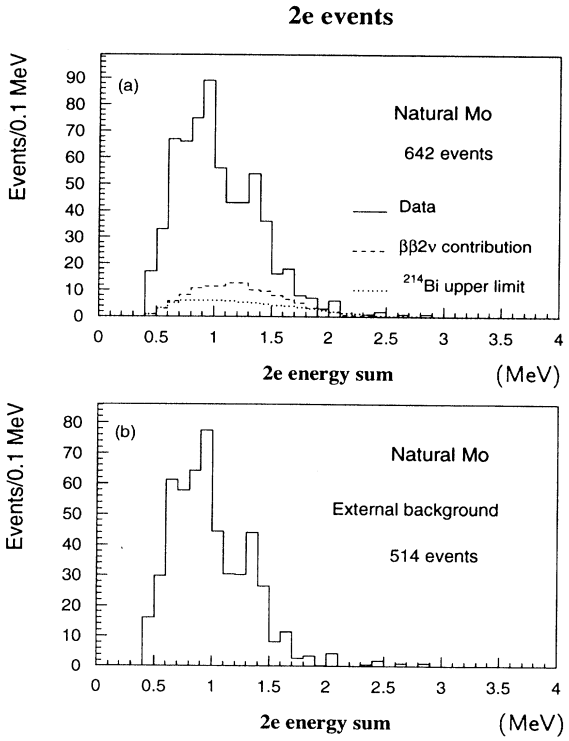

FIG. 9. Energy sum spectra. The raw data energy spectrum in natural molybdenum (a) is dominated by external background; the $\beta\beta2\nu$ decay contribution (dashed line) and the small amount of ^{214}Bi (dotted line) in the case of the calculated upper limit are indicated. The calculated external background spectrum (b) in this foil is the result of the subtraction of the $\beta\beta2\nu$ contribution. It is used to estimate the background in the enriched molybdenum foil.

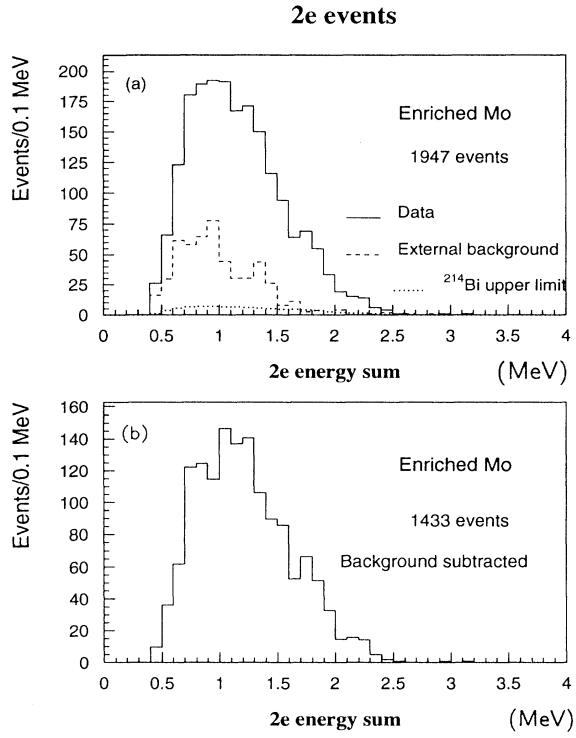

FIG. 10. Energy sum spectra. The raw data energy spectrum (solid line) in enriched molybdenum (a) is dominated by $\beta\beta2\nu$ decay and there are few events in the 3 MeV region. The very small contribution of ^{214}Bi (dotted line) corresponds to the upper limit 33 mBq/kg. The estimated external background spectrum is obtained from the natural molybdenum foil (see Fig. 9). After subtraction (b) the 2e energy sum spectrum contains 1433 events.

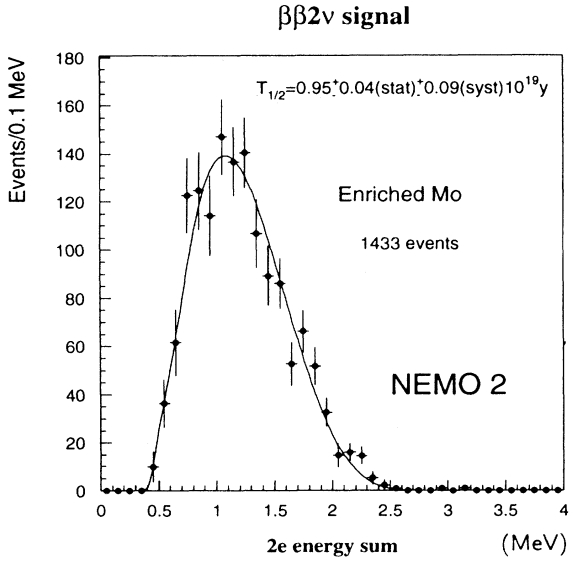

FIG. 11. Fit of the signal. The one-parameter fit of the histogram [Fig. 10(b)] is done with the χ^2 method ($\chi^2 = 19.2$ for 18 degrees of freedom). The quoted error bars take into account the subtraction procedure.

life be the adjustable parameter defined above gives the result

$$T_{1/2} = 0.95 \pm 0.04(\text{stat}) \pm 0.09(\text{syst})\ 10^{19}\ \text{yr}\ .$$

To ensure the validity of the Gaussian approximation only data bins with more than nine events were used in the fit. The error bars in the spectrum reflect the external background subtraction and the spectrum accurately depicts the simulated spectrum with a χ^2/degree of freedom of 1.1. The three main contributions to systematic uncertainties are derived from Monte Carlo calculations, detector performance, and data analysis.

In the simulation of low energy electrons, errors arise mainly from scattering computations which depend on the step size used for a given material in the detector. The step size in the GEANT simulation is an adjustable parameter which must be set such that the mean scattering angle is sufficiently small to accurately track the electrons. The step size has to be chosen ≤ 1 μm for electrons with energies of a few hundred keV in heavy materials such as molybdenum. Computations with a 0.1 μm step size change the efficiency, with respect to a 1 μm step, by 6% which is the value used for the systematic error.

The absolute energy calibration error for 200 keV electrons has been estimated to be 10 keV. Given this estimate and in accordance with the single-electron spectrum (of Fig. 13) one deduces an uncertainty of 45 2e events corresponding to a 3% systematic error in the signal. A small additional error arises from a 1% uncertainty in the fiducial source foil mass.

The data analysis introduces sources of error due to geometrical cuts and external and internal background subtractions. The geometrical cuts introduce a 2% error in the process of extrapolating electron tracks to triggered PMT's.

Errors in the estimates of external background are made in the use of the number of $e\gamma$ events in the two foils (Sec. IV A and Fig. 5) corrected for those calculated from the internal ^{214}Bi and ^{208}Tl contaminations (Sec. IV B). The efficiencies for producing $e\gamma$ events in the enriched molybdenum foil are, respectively, 4.1×10^{-3} and 6.9×10^{-3} for ^{214}Bi and ^{208}Tl. Of interest is the number of 2e events produced by second order processes which depends on the foil thickness. A 2e event ratio (enriched and natural molybdenum) of 1.12 is thus calculated which gives a difference of 62 2e events in the two foils. The ratio obtained in the 2e analysis is 1.0 (Sec. V) while a calculation using the mass thickness and efficiency of the two foils gives 0.98. The difference between the two estimated ratios (1.12 and 1.0) leads to a 4% systematic error for the external background subtraction.

The error in the internal background subtraction is estimated from the difference in $e\gamma$ events, within appropriate cuts (Sec. IV B), in the enriched and natural molybdenum. Given that less than 14 observed $e\gamma$ events, at the 90% C.L., are attributed to ^{214}Bi, a limit of 42 2e events has been calculated. Similarly the ^{208}Tl contribution is limited to 15 2e events. The hypothesis concerning

^{234m}Pa (Sec. IV B) contributes 41 events. These combine to present a 5% systematic uncertainty in the internal background subtraction. A total systematic error on the half-life of 9.5% is derived.

The distribution of the angle between the two electrons in enriched molybdenum (background subtracted) is also closely reproduced by the $\beta\beta2\nu$ simulations (Fig. 12) and is quite different from the distribution extracted from the natural molybdenum data. A cut on the angle α, between the two electrons, such as $\cos\alpha < 0.6$ increases, the signal-to-background ratio and a fit to the resultant energy spectrum (1064 events) gives a half-life of $T_{1/2} = 0.93 \times 10^{19}$ yr. This fit is very close to the previous one with practically the same errors.

Finally the single-electron energy spectra (Fig. 13) are very different for the signal and background. These differences and the agreement between enriched molybdenum data and simulation data are a strong argument for a $\beta\beta2\nu$ signal.

B. Half-life limits for 0ν modes

The $\cos\alpha < 0.6$ cut reduces the external background contributions and is applied to the following analysis

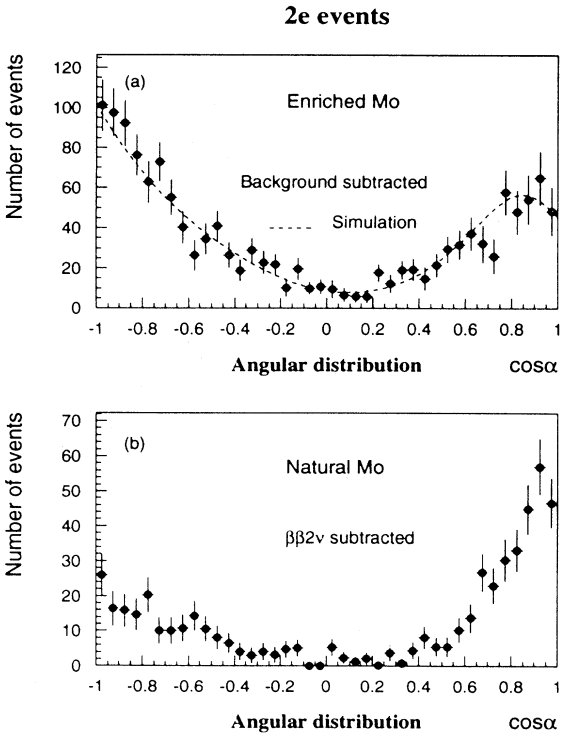

FIG. 12. Angular distributions. The angular distribution in enriched molybdenum (a) is in good agreement with the simulation (dashed line) using the measured half-life (α is the angle between the two electron directions). In natural molybdenum (b) the distribution has a very different behavior being peaked in the forward direction as expected from the external photon flux. In both cases the distributions are strongly distorted by detector geometry and by multiple scattering in the foils.

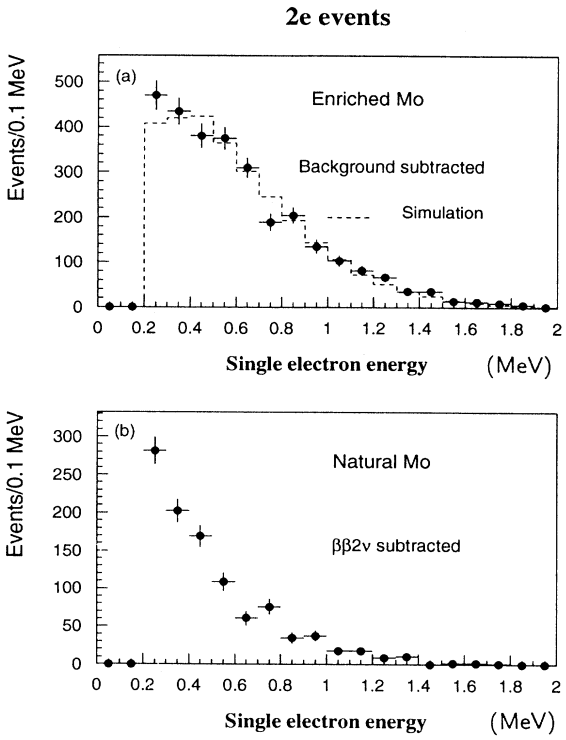

FIG. 13. Single-electron energy spectra. The energy distribution of single electrons in enriched molybdenum (a) is well reproduced by the simulation (dashed line) using the measured half-life. In natural molybdenum (b) the energy spectrum is much more peaked at low energy.

yielding an increase in the half-life limits of 30%. Limits were obtained using the formula for Poisson processes with background [13]:

$$\text{C.L.} = 1 - e^{-(\mu_s+N)} \sum_{n=0}^{n_0} \frac{(\mu_b+N)^n}{n!} \Big/ e^{-\mu_b} \sum_{n=0}^{n_0} \frac{{\mu_b}^n}{n!} ,$$

where μ_s is the signal expectation value, μ_b the known background expectation value, n_0 the number of observed events, and N the upper limit on μ_s at the confidence level (C.L.) Half-life limits have been computed at the 90% C.L. (see Table I) for the following $\beta\beta0\nu$ channels: $(0^+ \rightarrow 0^+_{GS})$ with and without Majoron emission,

TABLE I. Half-life limits (90% C.L.). For each channel a window in energy is defined, the corresponding number of experimental events, the number of calculated $\beta\beta2\nu$ events plus the external background one, the efficiency, and the half-life limit are given ($\cos\alpha < 0.6$).

Channel	0^+_{GS}	Majoron	2^+_1	0^+_1
Window (MeV)	[2.6,3.0]	[2.1,2.9]	[2.1,2.5]	[1.4,1.9]
Number of events	1	31	30	290
$\beta\beta2\nu$ + background	2.	25.	22.5	306.
Efficiency (%)	3.6	1.4	2.4	2.7
$T_{1/2}(10^{21}$ y)	>6.4	>0.5	>0.8	>0.6

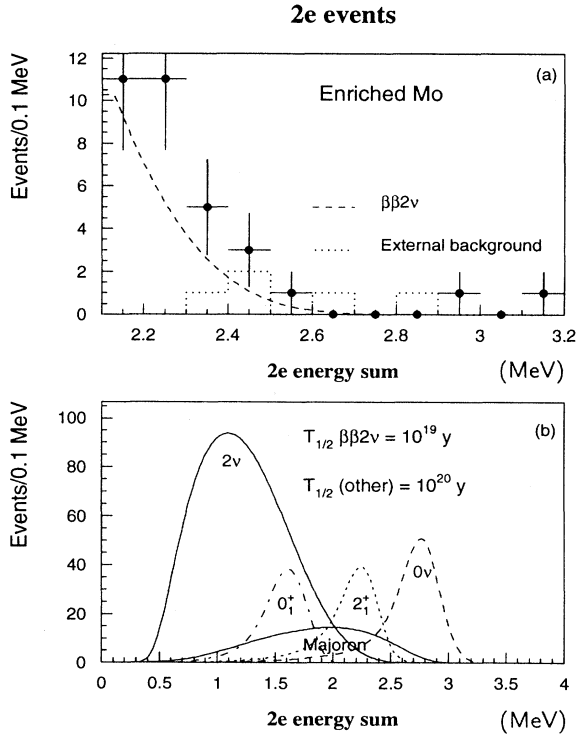

FIG. 14. Spectra used for limit computations. The high energy region of the fitted energy sum spectrum (a) shows clearly the numbers of expected and experimental events involved in the computation of the limits given in Table I. The curves referring to the different decay modes (b) considered in this analysis show the detector response and explain the energy domains used to compute the limits.

$(0^+ \rightarrow 2_1^+)$ and $(0^+ \rightarrow 0_1^+)$. In the case of the 0_1^+ state two photons are emitted (591 keV and 540 keV); the $2e$ energy sum cutoff is then 1.90 MeV. In the case of the 2_1^+ state one photon (540 keV) is emitted and the $2e$ energy sum cutoff is 2.49 MeV. In both cases photon detection is not required because of the small efficiencies.

For each channel the quoted energy range has been obtained by minimizing the background ($\beta\beta2\nu$+ external background) and maximizing the detection efficiency; simulations of these channels are shown in Fig. 14(b). An expanded view of the high energy part of the $2e$ spectrum [Fig. 14(a)] in enriched molybdenum and in natural molybdenum (external background) shows the $\beta\beta2\nu$ contribution.

VI. DISCUSSION AND CONCLUSION

The $\beta\beta2\nu$ decay result, $T_{1/2} = 0.95 \pm 0.04(\text{stat.}) \pm 0.09(\text{syst.})$ 10^{19} yr is in agreement with other experiments, $T_{1/2} = 1.15^{+0.3}_{-0.2}10^{19}y$ [14] and $T_{1/2} = 1.16^{+0.34}_{-0.08}10^{19}y$ [15], but the statistical significance of the data sample in this experiment is much higher. The angular distribution and the single energy spectrum are compared to simulated theoretical spectra.

The best published $\beta\beta0\nu$ limit for the half-life to the 0^+_{GS} mode is 4.4×10^{22} yr (68% C.L.) [16] and is somewhat higher than the limit derived here, 0.64×10^{22} yr (90% C.L.) or 1.2×10^{22} yr (68% C.L.). These limits have been performed with different statistical methods and thus direct comparison is complicated. Concerning the 2_1^+ excited state, the half-life limit obtained is 0.8×10^{21} yr (90% C.L.) and 1.1×10^{21} yr (68% C.L.); the best published value is 1.1×10^{21} yr (68% C.L.) [17]. The 0_1^+ excited state limit presented here is 0.6×10^{21} yr (90% C.L.) and is close to the limit 1.7×10^{21} yr (90% C.L.) [18]. Finally, for the case of Majoron emission there is a recently published limit of 7.9×10^{20} yr (68% C.L.) [19] which is practically the same as the limit presented here of 5×10^{20} yr (90% C.L.) or 7.5×10^{20} yr (68% C.L.).

Recent computations of matrix elements have been performed for the $\beta\beta2\nu$ mode [20–22] and for the $\beta\beta0\nu$ mode [20,22–24] in the ^{100}Mo isotope. Given the half-life obtained for the allowed process, in this experiment, a nuclear matrix element was computed, $M_{2\nu} = 0.11$, which is close to 0.13, the result of Ref. [20] with the phase space factor of 925.0×10^{-20} yr^{-1}.

The neutrinoless matrix elements $M_{0\nu}$ obtained by the quoted authors can vary by a factor of 3. Using the half-life limit deduced from our data, the lower limit of the effective neutrino mass is in the range: $\langle m_\nu \rangle < 6.0$–18.0 eV, with a phase space factor of 10.4×10^{-13} yr^{-1}. The best limit, $\langle m_\nu \rangle < 1.3$–3.2 eV, is given by a germanium experiment [25], using the matrix elements of Refs. [22–24,26]. A limit on the Majoron-neutrino coupling constant is derived from the results presented here and using the above referenced $M_{0\nu}$ and the phase space factor of 37.5×10^{-15} yr^{-1} one obtains $\langle g_M \rangle < 2.0$–$6.0\times10^{-4}$. The germanium experimental limit [27] calculated with the already referenced matrix elements is $\langle g_M \rangle < 1.6$–$4.3 \times 10^{-4}$.

The NEMO 2 detector built for background studies has provided important physics. A very low $2e$ background has been observed in the 3 MeV region. Data collection with molybdenum has been completed but the NEMO 2 detector continues to run with upgraded scintillators and PMT's in order to advance the photon tagging efficiency and to measure the source activity. This research will be applied to the final design of NEMO 3.

ACKNOWLEDGMENTS

The authors would like to thank the Fréjus Underground Laboratory staff for their technical assistance in running the experiment.

[1] D. Dassié *et al.*, Nucl. Instrum. Methods A **309**, 465 (1991).

[2] NEMO Collaboration, D. Dassié, in *TAUP '91*, Proceedings of the Second International Workshop on Theoretical and Phenomenological Aspects of Underground Physics, Toledo, Spain, 1991, edited by A. Morales, J. Morales, and J. Villar [Nucl. Phys. B (Proc. Suppl.) **28A**, 223 (1992)].

[3] NEMO Collaboration, D. Dassié, Nucl. Instrum. Methods A **354**, 338 (1995).
[4] NEMO Collaboration, in *Proceedings of the International Europhysics Conference on High Energy Physics*, Marseille, France, 1993, edited by J. Carr and M. Perrottet (Editions Frontieres, Gif-sur-Yvette, 1993), p. 545.
[5] NEMO Collaboration, in *TAUP 93*, Proceedings of the Third International Workshop on Theoretical and Phenomenological Aspects of Underground Physics, Gran Sasso, Italy, 1993, edited by C. Arpesella, E. Belloti, and A. Bottino [Nucl. Phys. B (Proc. Suppl.) **35**, 369 (1994)].
[6] NEMO Collaboration, in *TAUP 91* [2], p. 425.
[7] J.E Campagne *et al.*, in *Progress in Atomic Physics Neutrinos and Gravitation*, Proceedings of the XIIth Moriond Workshop, 1992, edited by G. Chardin, O. Fackler, and J. Trân Thanh Vân (Editions Frontiéres, Gif-sur-Yvette, 1992), p. 189.
[8] P. Billoir, Nucl. Instrum. Methods A **225**, 352 (1984).
[9] "GEANT simulation program," GEANT CERN Program Library Q123, 1993, Report No. CERN-DD/EE/84/1 (unpublished).
[10] M. Doi *et al.*, Prog. Theor. Phys. **66**, 1739 (1981).
[11] C.M. Lederer and V.S. Shirley, *Table of Isotopes*, 7th ed. (Wiley, New York, 1978).
[12] "PAW, Physics Analysis Workstation," CERN Program Library Entry Q121, CERN, 1993 (unpublished).
[13] O. Helene, Nucl. Instrum. Methods B **212**, 319 (1983); Particle Data Group, K. Hikasa *et al.* Phys. Rev. D **45**, S1 (1992).
[14] H. Ejiri *et al.*, Phys. Lett. B **258**, 17 (1991).
[15] S.R. Elliott *et al.*, J. Phys. G. **17**, S145 (1991).
[16] M. Alston-Garnjost *et al.*, Phys. Rev. Lett. **71**, 831 (1993).
[17] N. Kudomi *et al.*, Phys. Rev. C **46**, 2132 (1992).
[18] A.S. Barabash *et al.*, in *Proceeding of the IIIrd International Symposium on Weak and Electroweak Interactions in Nuclei*, Dubna, Russia, 1992, edited by Ts.D. Vylov (World Scientific, Singapore, 1993), p. 582.
[19] H. Ejiri *et al.*, Phys. Rev. D **48**, 5412 (1993).
[20] J. Engel, P. Vogel, and M.R. Zirnbauer, Phys. Rev. C **37**, 731 (1988).
[21] X.R. Wu *et al.*, Phys. Lett. B **272**, 169 (1991).
[22] K. Muto, E. Bender, and H.V. Klapdor, Z. Phys. A **334**, 177 (1989); **334**, 187 (1989).
[23] T. Tomoda, Rep. Prog. Phys. **54**, 53 (1991).
[24] G. Pantis, A. Faessler, W.A. Kaminski, and J.D. Vergados, J. Phys. G **18**, 605 (1992).
[25] A. Balysh *et al.*, Phys. Lett. B **283**, 32 (1992).
[26] M. Moe and P. Vogel, Report No. UCI-Neutrino 94-5 (unpublished).
[27] M. Beck *et al.*, Phys. Rev. Lett. **70**, 2853 (1993).